

Shining Light on Dark Matter,
One Photon at a Time

by

Brandon Leigh Allen

Submitted to the Department of Physics
in partial fulfillment of the requirements for the degree of

Doctorate of Science in Physics

at the

MASSACHUSETTS INSTITUTE OF TECHNOLOGY

June 2019

© Massachusetts Institute of Technology 2019. All rights reserved.

Author
Department of Physics
May 18, 2019

Certified by
Christoph E.M. Paus
Professor
Thesis Supervisor

Accepted by
Nergis Mavalvala
Associate Department Head for Education

Shining Light on Dark Matter, One Photon at a Time

by

Brandon Leigh Allen

Submitted to the Department of Physics
on May 18, 2019, in partial fulfillment of the
requirements for the degree of
Doctorate of Science in Physics

Abstract

A search is conducted for new physics in final states containing a photon and missing transverse momentum in proton-proton collisions at $\sqrt{s} = 13$ TeV. The data collected by the CMS experiment at the CERN LHC correspond to an integrated luminosity of 35.9 inverse femtobarns. No deviations from the predictions of the standard model are observed. The results are interpreted in the context of dark matter production and limits on new physics parameters are calculated at 95% confidence level. For the two simplified dark matter production models considered, the observed (expected) lower limits on the mediator masses are both 950 (1150) GeV for 1 GeV dark matter mass.

Thesis Supervisor: Christoph E.M. Paus
Title: Professor

Acknowledgments

This is the acknowledgements section. You should replace this with your own acknowledgements.

Contents

1	The Monophoton Analysis	15
1.1	Event Selection	15
1.2	Irreducible backgrounds	15
1.2.1	Higher-order corrections to $V+\gamma$ differential cross sections . .	17
1.3	Misidentified electrons	17
1.4	Misidentified hadrons	19
1.5	Spikes	25
1.6	Beam halo	25
1.7	Other minor SM background processes	26
1.8	Statistical Interpretation	27
1.9	Results	30
1.9.1	Pre-fit and post-fit distributions	30
1.9.2	Limits	32
2	Comparison with Other Results	35
2.1	Monophoton	35
2.2	Monojet / Mono- Z	35
2.3	Direct Detection	35
2.4	Indirect Detection	35

List of Figures

- 1-1 Transfer factors $R_{ee\gamma}^{Z\gamma}$ (left) and $R_{\mu\mu\gamma}^{Z\gamma}$ (right). The uncertainty bands in green (inner) and orange (outer) show the systematic uncertainty, and the combination of systematic and statistical uncertainty arising from limited MC sample size, respectively. The systematic uncertainties considered are the uncertainties in the data-to-simulation correction factors ρ for the lepton identification efficiencies. 15
- 1-2 Transfer factors $R_{e\gamma}^{W\gamma}$ (left) and $R_{\mu\gamma}^{W\gamma}$ (right). The uncertainty bands in green (inner) and orange (outer) show the systematic uncertainty, and the combination of systematic and statistical uncertainty arising from limited MC sample size, respectively. The systematic uncertainties considered are the uncertainties in the data-to-simulation correction factors ρ for the lepton identification efficiencies. 16
- 1-3 Transfer factor $f_{W\gamma}^{Z\gamma}$. The uncertainty bands in green (inner) and orange (outer) show the systematic uncertainty, and the combination of systematic and statistical uncertainty arising from limited MC sample size, respectively. The systematic uncertainties considered are the uncertainties from higher-order theoretical corrections. 17
- 1-4 Electroweak NLO cross section corrections as a function of photon p_T for $Z(\rightarrow \nu\bar{\nu})+\gamma$ (top), $W^++\gamma$ (bottom left), and $W^-+\gamma$ (bottom right) processes, overlaid with uncertainty bands. See text for descriptions of the individual components of the uncertainty. The uncertainty due to γ -induced production is negligible in $Z(\rightarrow \nu\bar{\nu})+\gamma$ production. 18

1-5	Systematic uncertainty in the transfer factors for $Z(\rightarrow \nu\bar{\nu})+\gamma$ (left) and $W(\rightarrow \ell\nu)+\gamma$ (right). The last bin includes all events with $E_T^\gamma > 1000$ GeV.	19
1-6	Fits to the mass distributions for ee (left) and $e\gamma$ (right) selections, in bins of probe p_T : $175 < p_T < 200$ GeV (top), $200 < p_T < 250$ GeV (middle), $p_T > 250$ GeV (bottom). The blue solid line represents the full fit model, and the green dashed line its background component.	20
1-7	Electron to photon fake rate R_e	21
1-8	Impurities for photons as a function of p_T . The different bands show the effects of adding different stages of the full ID, starting with the baseline ID and isolation and successively adding the pixel seed veto.	22
1-9	Left: The p_T distribution of the candidate photon object in the photon + jet control sample (black), the result of scaling it with the impurity (red), and the p_T distribution of the hadronic proxy object in the proxy + jet control sample (blue). Right: Hadronic transfer factor R_h , which is the ratio of the red and blue distributions in the left plot. Top: Nominal hadron proxy object. Middle: Tighter hadron proxy object. Bottom: Looser hadron proxy object.	23
1-10	The p_T distribution of the estimated contribution from hadronic fakes in the signal region. The distribution labeled Up (Down) comes from the tighter (looser) selection. The systematic uncertainty resulting from this variation is around 5% at the low end of our p_T range and increases to 15% after $p_T > 400$ GeV.	24
1-11	The p_T distribution of the estimated contribution from hadronic fakes in the signal region. The distribution labeled Up (Down) comes from varying the purity one sigma up (down). The systematic uncertainty resulting from this variation is around 5% at the low end of the p_T range and increases to 20% after $p_T > 400$ GeV.	25
1-12	Folded ϕ' distribution of the halo sample.	26

1-13 Comparison between data and MC simulation in the four control regions: $ee\gamma$ (upper left), $\mu\mu\gamma$ (upper right), $e\gamma$ (lower left), $\mu\gamma$ (lower right) before and after performing the simultaneous fit across all the control samples and signal region, and assuming absence of any signal. The last bin of the distribution includes all events with $E_T^\gamma > 1000$ GeV. The ratios of data with the pre-fit background prediction (red dashed) and post-fit background prediction (blue solid) are shown in the lower panels. The bands in the lower panels show the post-fit uncertainty after combining all the systematic uncertainties. 28

1-14 Observed E_T^γ distributions in the horizontal (left) and vertical (right) signal regions compared with the post-fit background expectations for various SM processes. The last bin of the distribution includes all events with $E_T^\gamma > 1000$ GeV. The expected background distributions are evaluated after performing a combined fit to the data in all the control samples and the signal region. The ratios of data with the pre-fit background prediction (red dashed) and post-fit background prediction (blue solid) are shown in the lower panels. The bands in the lower panels show the post-fit uncertainty after combining all the systematic uncertainties. The expected signal distribution from a 1 TeV vector mediator decaying to 1 GeV DM particles is overlaid. 29

1-15 Covariances between the predicted background yields in all the E_T^γ bins of the horizontal and vertical signal regions. The bin labels specify which signal region the bin belongs to and what number bin it is for that region. 31

1-16	The ratio of 95% CL upper cross section limits to the theoretical cross section (μ_{95}), for DM simplified models with vector (left) and axial-vector (right) mediators, assuming $g_q = 0.25$ and $g_{\text{DM}} = 1$. Expected $\mu_{95} = 1$ contours are overlaid in red. The region under the observed contour is excluded. For DM simplified model parameters in the region below the lower violet dot-dash contour, and also above the corresponding upper contour in the right hand plot, cosmological DM abundance exceeds the density observed by the Planck satellite experiment.	33
2-1	The 90% CL exclusion limits on the χ -nucleon spin-independent scattering cross sections involving the vector operator as a function of the m_{DM} . Simplified model DM parameters of $g_q = 0.25$ and $g_{\text{DM}} = 1$ are assumed. The region to the upper left of the contour is excluded. On the plots, the median expected 90% CL curve overlaps the observed 90% CL curve. Also shown are corresponding exclusion contours, where regions above the curves are excluded, from the recent results by the CDMSLite [?], LUX [?], PandaX-II [?], XENON1T [?], and CRESST-II [?].	36
2-2	The 90% CL exclusion limits on the χ -nucleon spin-dependent scattering cross sections involving the axial-vector operator as a function of the m_{DM} . Simplified model DM parameters of $g_q = 0.25$ and $g_{\text{DM}} = 1$ are assumed. The region to the upper left of the contour is excluded. On the plots, the median expected 90% CL curve overlaps the observed 90% CL curve. Also shown are corresponding exclusion contours, where regions above the curves are excluded, from the recent results by the PICO-60 [?], IceCube [?], PICASSO [?] and Super-Kamiokande [?] Collaborations.	36

List of Tables

1.1	Impurities for photons as a function of p_T	21
1.2	Expected event yields in each E_T^γ bin for various background processes in the horizontal signal region. The background yields and the corresponding uncertainties are obtained after performing a combined fit to data in all the control samples, excluding data in the signal region. The observed event yields in the horizontal signal region are also reported.	30
1.3	Expected event yields in each E_T^γ bin for various background processes in the vertical signal region. The background yields and the corresponding uncertainties are obtained after performing a combined fit to data in all the control samples, excluding data in the signal regions. The observed event yields in the vertical signal region are also reported.	32

Chapter 1

The Monophoton Analysis

The main event.

1.1 Event Selection

1.2 Irreducible backgrounds

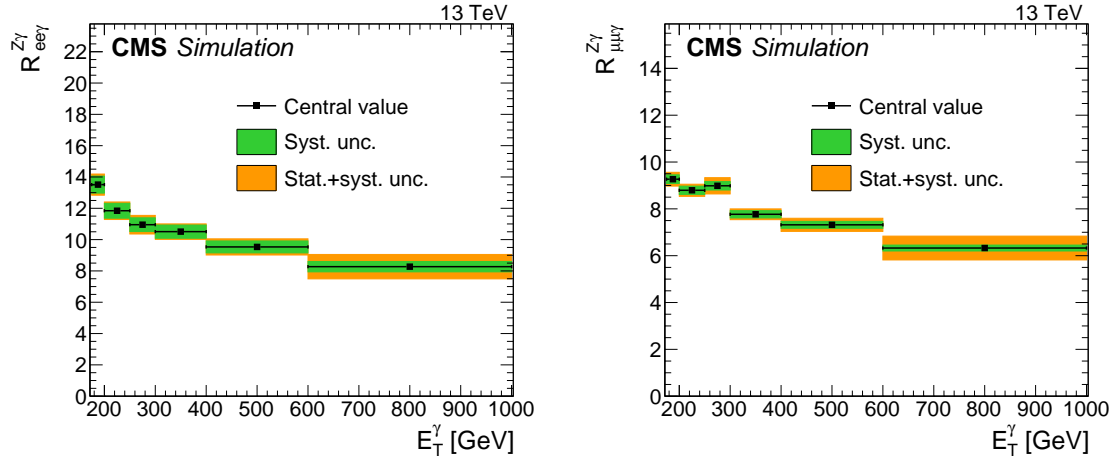


Figure 1-1: Transfer factors $R_{ee\gamma}^{Z\gamma}$ (left) and $R_{\mu\mu\gamma}^{Z\gamma}$ (right). The uncertainty bands in green (inner) and orange (outer) show the systematic uncertainty, and the combination of systematic and statistical uncertainty arising from limited MC sample size, respectively. The systematic uncertainties considered are the uncertainties in the data-to-simulation correction factors ρ for the lepton identification efficiencies.

Using the transfer factor $R_{\ell\ell\gamma}^{Z\gamma}$, the total estimated event yield $T_{\ell\ell\gamma}$ in each dilepton control region in the i^{th} bin of the E_T^γ distribution can be expressed as

$$T_{\ell\ell\gamma,i} = \frac{N_i^{Z\gamma}}{R_{\ell\ell\gamma,i}^{Z\gamma}} + b_{\ell\ell\gamma,i}, \quad (1.1)$$

where $N^{Z\gamma}$ is the number of $Z(\rightarrow \nu\bar{\nu})+\gamma$ events in the combined signal regions and $b_{\ell\ell\gamma}$ is the predicted contribution from other background sources in the dilepton control region, namely $t\bar{t}\gamma$, $VV\gamma$, and misidentified hadrons. The subscript i indicates that the quantities are evaluated in bin i of the E_T^γ distribution.

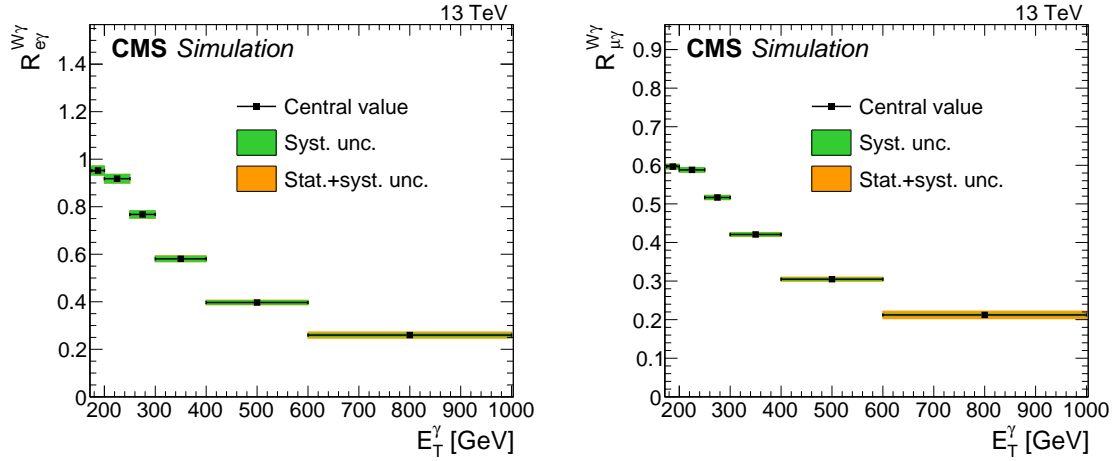


Figure 1-2: Transfer factors $R_{e\gamma}^{W\gamma}$ (left) and $R_{\mu\gamma}^{W\gamma}$ (right). The uncertainty bands in green (inner) and orange (outer) show the systematic uncertainty, and the combination of systematic and statistical uncertainty arising from limited MC sample size, respectively. The systematic uncertainties considered are the uncertainties in the data-to-simulation correction factors ρ for the lepton identification efficiencies.

Using $R_{\ell\gamma}^{W\gamma}$ and $f_{W\gamma}^{Z\gamma}$, the total estimated event yield $T_{\ell\gamma}$ in each single-lepton control region in the i^{th} bin of the E_T^γ distribution can be expressed as

$$T_{\ell\gamma,i} = \frac{N_i^{Z\gamma}}{R_{\ell\gamma,i}^{W\gamma} f_{W\gamma,i}^{Z\gamma}} + b_{\ell\gamma,i}, \quad (1.2)$$

where $b_{\ell\gamma}$ is the predicted contribution from other background sources in the single-lepton regions, namely misidentified electrons and hadrons and other minor SM processes.

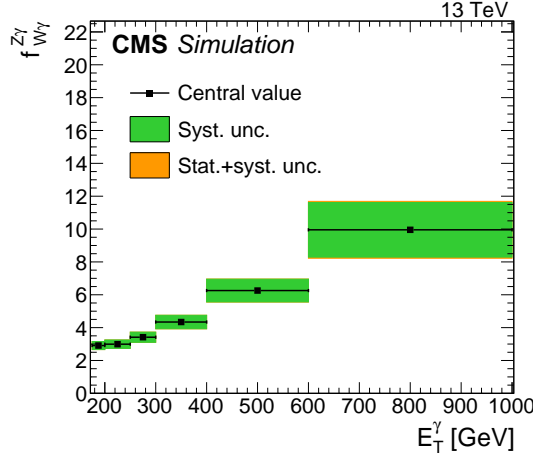


Figure 1-3: Transfer factor $f_{W\gamma}^{Z\gamma}$. The uncertainty bands in green (inner) and orange (outer) show the systematic uncertainty, and the combination of systematic and statistical uncertainty arising from limited MC sample size, respectively. The systematic uncertainties considered are the uncertainties from higher-order theoretical corrections.

1.2.1 Higher-order corrections to $V+\gamma$ differential cross sections

We apply the correction factors shown in Fig. 1-4, which are combinations of Sudakov suppression factors and photon-induced enhancements, and are provided by the authors of Ref. [?] in addition to the NNLO QCD correction.

Figure 1-5 shows the effect of systematic uncertainty in the ratio between the $Z(\rightarrow \nu\bar{\nu})+\gamma$ and $W(\rightarrow \ell\nu)+\gamma$ processes with respect to nominal value for $Z\gamma$ and $W\gamma$ respectively.

1.3 Misidentified electrons

Figure 1-6 shows the six fits performed on ee and $e\gamma$ in bins of probe p_T , from which the R_e factor used for the estimation of the electron misidentification background is derived. The R_e factor is computed as the ratio of the integral of the signal template function between 81 GeV and 101 GeV.

The proxy sample for the background estimation is obtained by identical event

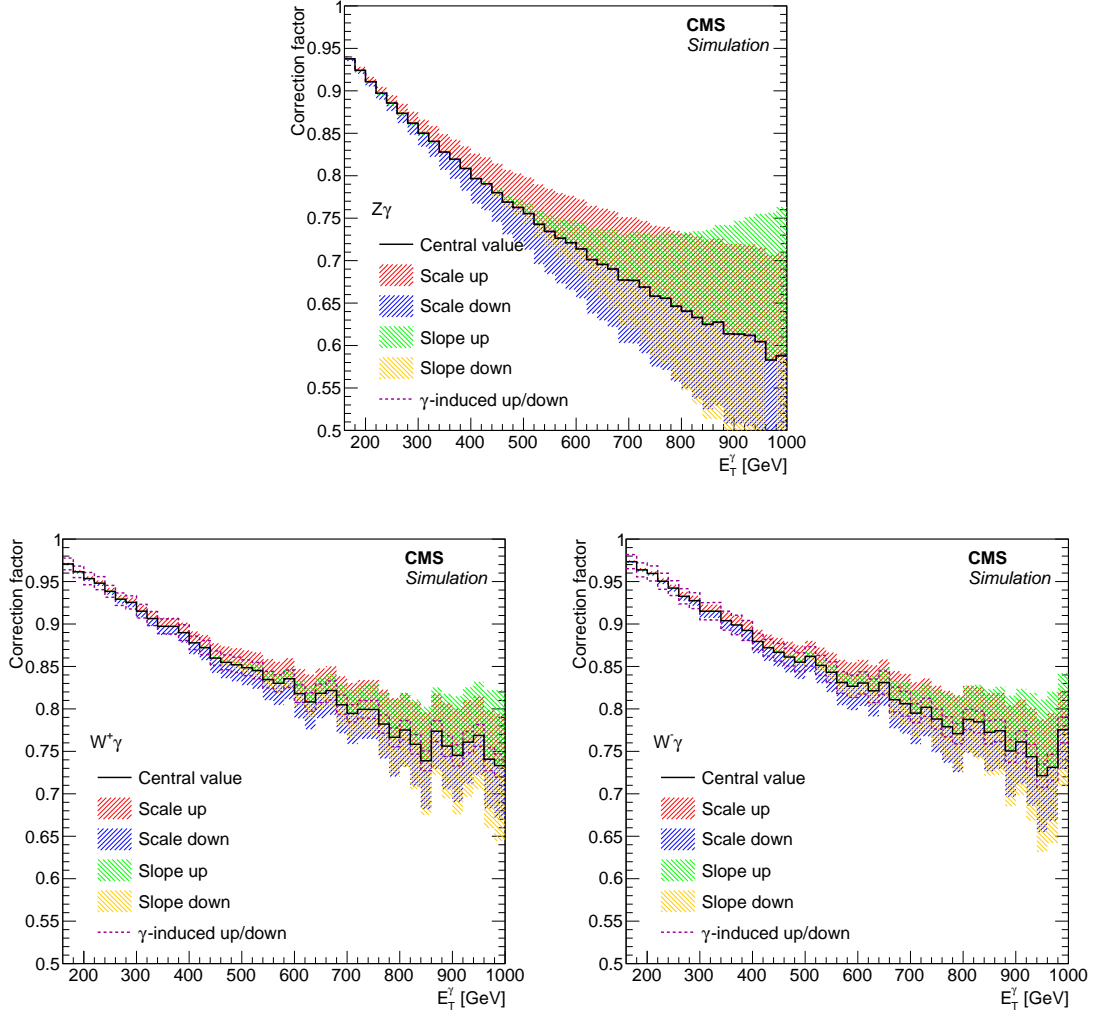


Figure 1-4: Electroweak NLO cross section corrections as a function of photon p_T for $Z(\rightarrow \nu\bar{\nu})+\gamma$ (top), $W^+ + \gamma$ (bottom left), and $W^- + \gamma$ (bottom right) processes, overlaid with uncertainty bands. See text for descriptions of the individual components of the uncertainty. The uncertainty due to γ -induced production is negligible in $Z(\rightarrow \nu\bar{\nu})+\gamma$ production.

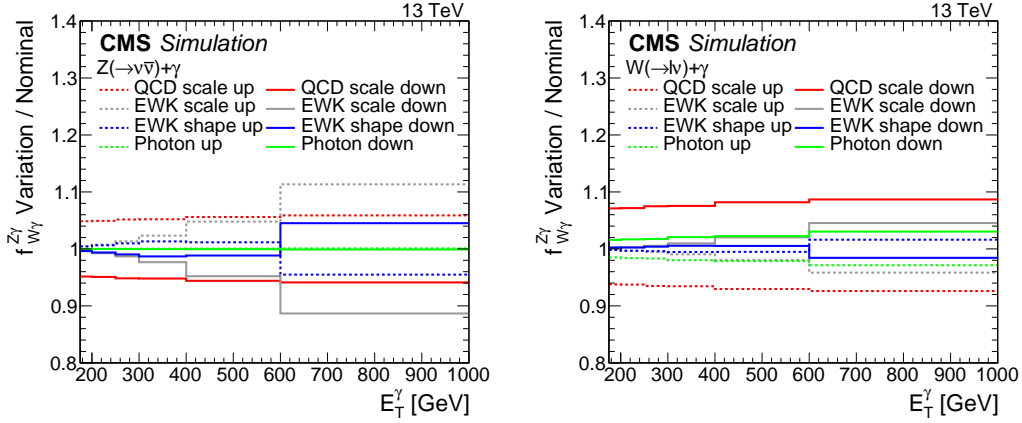


Figure 1-5: Systematic uncertainty in the transfer factors for $Z(\rightarrow \nu\bar{\nu})+\gamma$ (left) and $W(\rightarrow \ell\nu)+\gamma$ (right). The last bin includes all events with $E_T^\gamma > 1000$ GeV.

selection as that described in Sec. ??, but with the pixel-seed veto inverted on the photon candidate object.

Figure 1-7 shows the derived R_e factor as a function of E_T^γ . The electron proxy sample is reweighted by R_e depending on the p_T of the electron object.

1.4 Misidentified hadrons

The estimation of hadron misidentification background proceeds in multiple steps. First, the fraction of hadronic objects within a pool of photon candidate objects in the photon plus jet control region is measured. This measurement is described in detail in Section ?? . Figure 1-8 and Table 1.1 show the final impurity and associated uncertainties as a function of p_T .

Following this measurement, another control sample is formed where the photon in the photon plus jet sample is replaced by a hadronic proxy object. The hadronic proxy object is a reconstructed photon object which pass the photon ID described in Section ?? with the exception of failing at least one of the following cuts:

- $\sigma_{i\eta i\eta} < 0.01022$
- PF Charged Hadron isolation < 0.441 GeV .

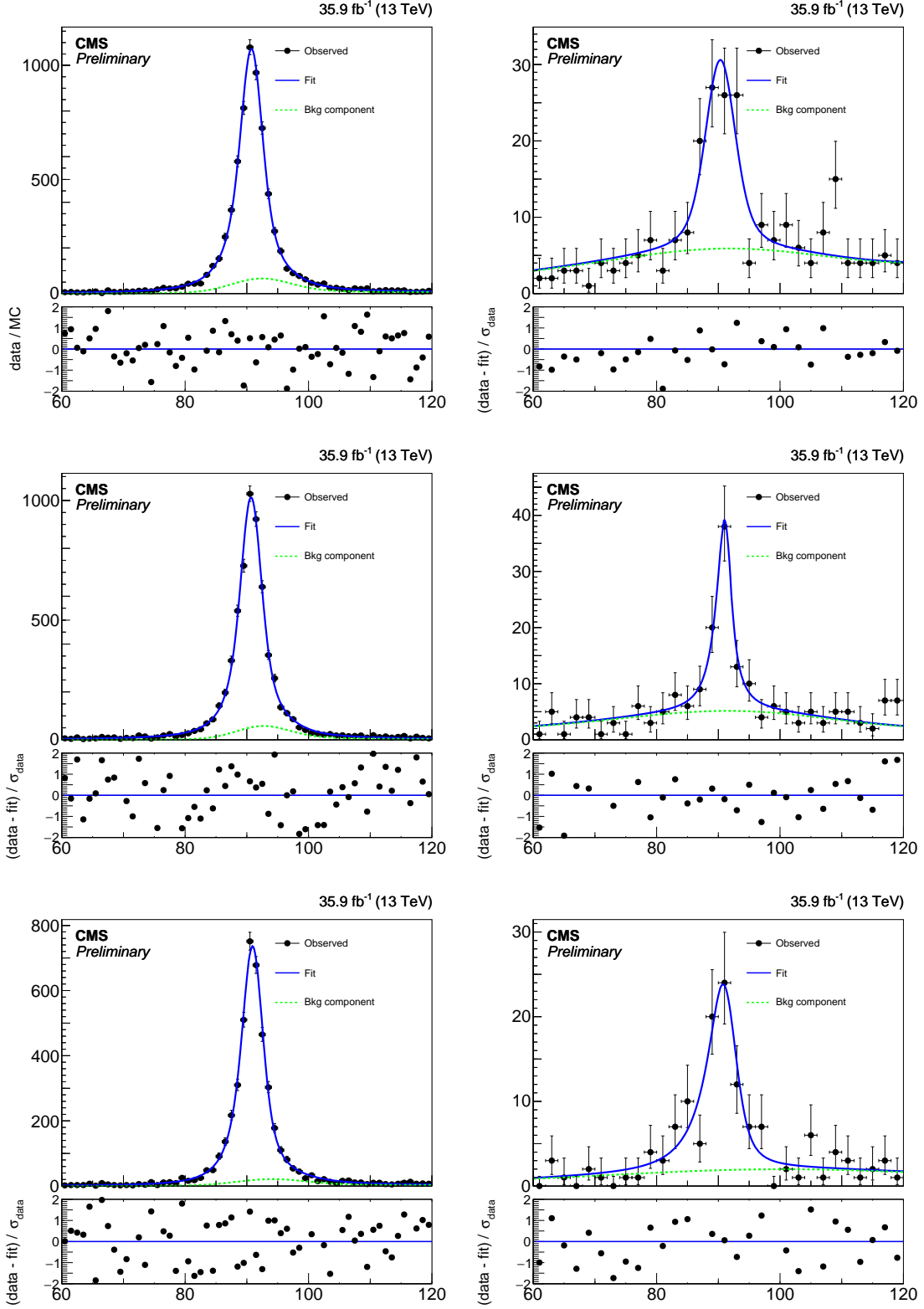


Figure 1-6: Fits to the mass distributions for ee (left) and $e\gamma$ (right) selections, in bins of probe p_T : $175 < p_T < 200$ GeV (top), $200 < p_T < 250$ GeV (middle), $p_T > 250$ GeV (bottom). The blue solid line represents the full fit model, and the green dashed line its background component.

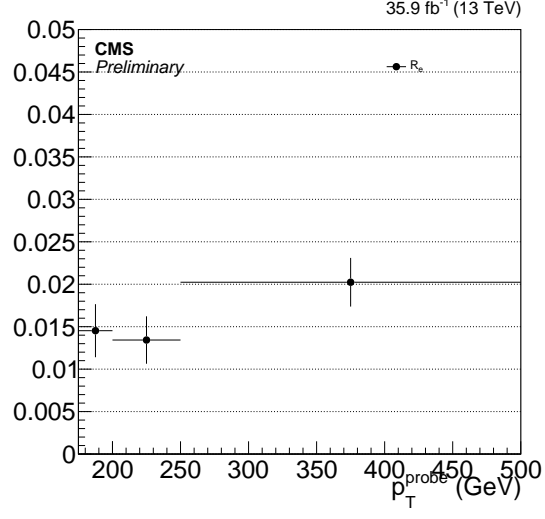


Figure 1-7: Electron to photon fake rate R_e .

Impurity (%) for barrel medium-pixel-monoph photons in data					
p_T Range (GeV)	Nominal	Sources of Systematic Uncertainty			
		Sideband	CH Iso Shape	Signal Shape	Bgkd. Stats
(175, 200)	4.31 ± 0.21	0.09	0.18	0.05	0.04
(200, 250)	3.39 ± 0.17	0.01	0.16	0.06	0.03
(250, 300)	2.44 ± 0.22	0.14	0.16	0.06	0.05
(300, 350)	1.99 ± 0.23	0.12	0.16	0.07	0.08
(350, 400)	1.43 ± 0.28	0.23	0.11	0.05	0.10
(400, ∞)	0.63 ± 0.30	0.27	0.09	0.05	0.05

Table 1.1: Impurities for photons as a function of p_T .

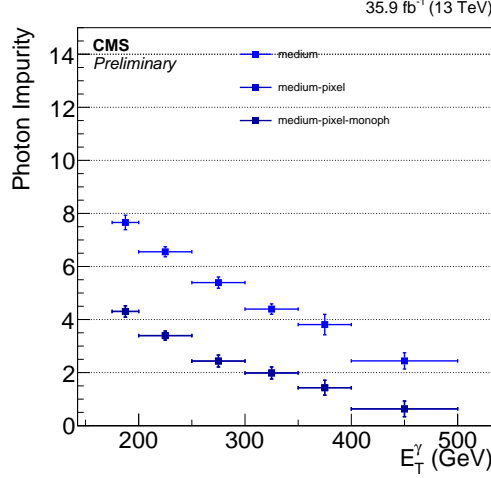


Figure 1-8: Impurities for photons as a function of p_T . The different bands show the effects of adding different stages of the full ID, starting with the baseline ID and isolation and successively adding the pixel seed veto.

Additionally, we apply a $E_T^{\text{miss}} < 60$ GeV cut to make this region orthogonal to the signal region of the analysis.

The hadronic transfer factor R_h , which measures the rate at which hadronic proxy objects result in hadrons that are misidentified as candidate photons, is obtained by dividing the estimated number of misidentified hadrons in the photon plus jet sample by the number of events in the hadron proxy + jet control region as a function of p_T . Figure 1-9 shows the transfer factor R_h along with the various distributions used for its derivation.

Finally, a third control sample of events with a hadronic proxy object and $E_T^{\text{miss}} > 170$ GeV is prepared. Under the assumption that the R_h stays constant regardless of whether the event has a high- p_T jet or E_T^{miss} , this proxy plus E_T^{miss} sample is then weighted by R_h to arrive at an estimate of the misidentified hadron plus E_T^{miss} background of this analysis.

To estimate the uncertainty on this background, we repeat the above method using tighter and looser definitions of the hadron proxy object. The tighter definition differs from the nominal by the following cuts:

- ρ -corrected PF Neutral Hadron isolation $< 0.264 + 0.014 \times p_T^\gamma + 0.000019 \times (p_T^\gamma)^2$.

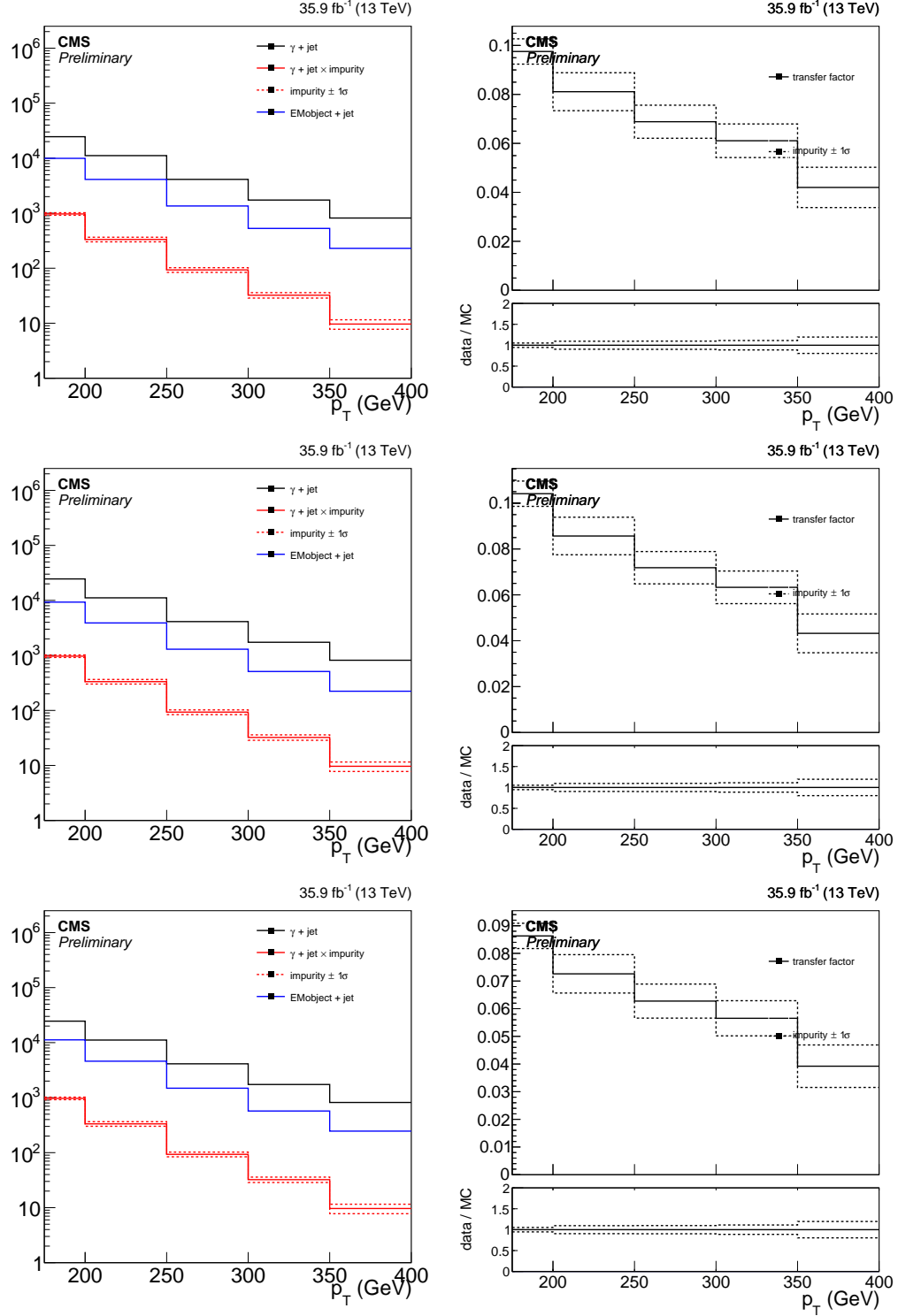


Figure 1-9: Left: The p_T distribution of the candidate photon object in the photon + jet control sample (black), the result of scaling it with the impurity (red), and the p_T distribution of the hadronic proxy object in the proxy + jet control sample (blue). Right: Hadronic transfer factor R_h , which is the ratio of the red and blue distributions in the left plot. Top: Nominal hadron proxy object. Middle: Tighter hadron proxy object. Bottom: Looser hadron proxy object.

- ρ -corrected PF Photon isolation $< 2.362 + 0.0053 \times p_T^\gamma$,

and the looser definition differs from the nominal by the following cuts:

- ρ -corrected PF Neutral Hadron isolation $< 10.910 + 0.014 \times p_T^\gamma + 0.000019 \times (p_T^\gamma)^2$.
- ρ -corrected PF Photon isolation $< 3.630 + 0.0053 \times p_T^\gamma$.

The different distributions from the nominal, tight, and loose selections are shown in Figure 1-10. The tight and loose shapes are taken as the one sigma band around the nominal estimate. Additionally, there is an uncertainty coming from the estimation of the photon purity. Figure 1-11 shows the resulting shapes from moving the shapes generated by a one sigma shift in the purity.

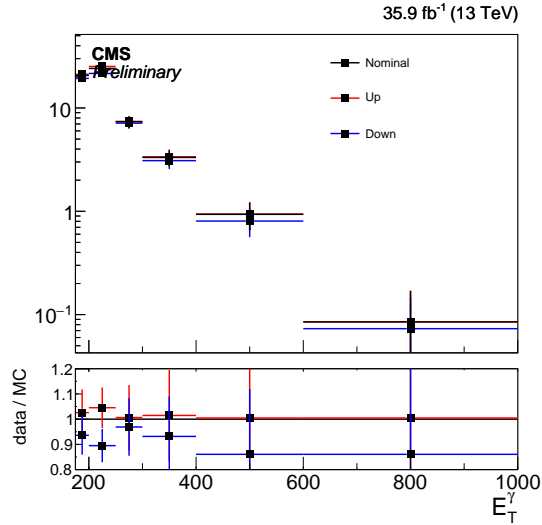


Figure 1-10: The p_T distribution of the estimated contribution from hadronic fakes in the signal region. The distribution labeled Up (Down) comes from the tighter (looser) selection. The systematic uncertainty resulting from this variation is around 5% at the low end of our p_T range and increases to 15% after $p_T > 400$ GeV.

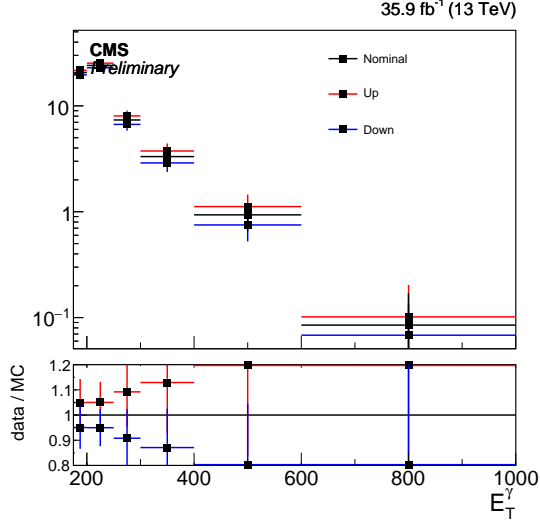


Figure 1-11: The p_T distribution of the estimated contribution from hadronic fakes in the signal region. The distribution labeled Up (Down) comes from varying the purity one sigma up (down). The systematic uncertainty resulting from this variation is around 5% at the low end of the p_T range and increases to 20% after $p_T > 400$ GeV.

1.5 Spikes

1.6 Beam halo

Figure 1-12 shows the ϕ distribution of the halo showers obtained from the single photon data set, requiring $E_T^\gamma > 175$ GeV and $E_T^{\text{miss}} > 170$ GeV. Here, halo showers are defined as photon objects that fail the MIP total energy cut in events where beam halo MET filter (one component of the “MET filters” mentioned in Section ??). The distribution is shifted and folded to make the peaking behavior clear. The resulting variable on the horizontal axis is named ϕ' .

The splitting of the signal region can be thought of as a two-bin fit. Collision processes occupy the relative fractions of phase space in the horizontal (H) and vertical (V) signal regions, $C_H = 1/\pi$ and $C_V = (\pi - 1)/\pi$, respectively. The corresponding fractions for beam halo events are determined by selecting a halo-enriched sample where the halo identification is inverted. Thus, a fit of the two signal regions provides an estimate of the overall normalization of the beam halo background, denoted h .

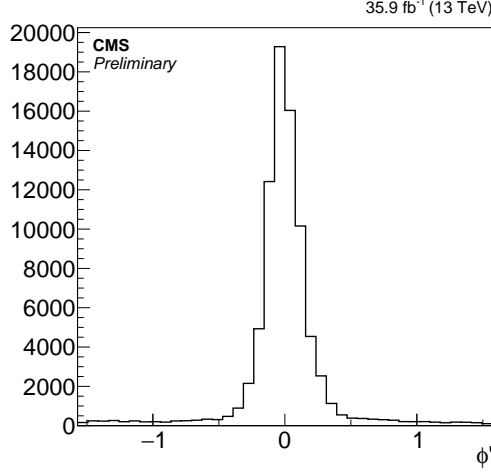


Figure 1-12: Folded ϕ' distribution of the halo sample.

The E_T^γ dependence of the halo background is encoded in $n_{K,i}^{\text{halo}}$, the unit-normalized beam halo prediction in the i^{th} bin of the signal region $K \in \{H, V\}$. Using the notation introduced in Section 1.2, the total estimated background T_K in the two signal regions are

$$\begin{aligned} T_{K,i} &= C_K(N_i^{Z\gamma} + N_i^{W\gamma}) + hn_{K,i}^{\text{halo}} + C_K b_{K,i} \\ &= C_K(1 + f_{W\gamma i}^{Z\gamma -1})N_i^{Z\gamma} + hn_{K,i}^{\text{halo}} + C_K b_{K,i}, \end{aligned} \quad (1.3)$$

where $b_{K,i}$ is the total contribution to bin i of region K from electron and hadron misidentification, ECAL spikes, and other minor SM background processes.

1.7 Other minor SM background processes

The SM $t\bar{t}\gamma$, $VV\gamma$, $Z(\rightarrow \ell\bar{\ell})+\gamma$, $W \rightarrow \ell\nu$, and γ +jets processes are minor ($\sim 10\%$) background processes in the signal region. Although $Z(\rightarrow \ell\bar{\ell})+\gamma$ and γ +jets do not involve high- p_T invisible particles, the former can exhibit large E_T^{miss} when the leptons fail to be reconstructed, and the latter when jet energy is severely mismeasured. The estimates for all five processes are taken from MADGRAPH5_aMC@NLO simulations at LO in QCD and can be found in Tables 1.2 and 1.3.

1.8 Statistical Interpretation

Free parameters of the fit are the yield of $Z(\rightarrow \nu\bar{\nu})+\gamma$ background in each bin of the signal regions ($N_i^{Z\gamma}$) and the overall normalization of the beam halo background (h). Bin-by-bin yields of $W(\rightarrow \ell\nu)+\gamma$ and $Z(\rightarrow \ell\bar{\ell})+\gamma$ samples in all regions are related to the yield of $Z(\rightarrow \nu\bar{\nu})+\gamma$ through the MC prediction through the transfer factors defined in Section 1.2. The transfer factors are allowed to shift within the aforementioned theoretical and experimental uncertainties.

The background-only likelihood that is maximized in the fit is

$$\begin{aligned}
\mathcal{L} &= \prod_i \{ \mathcal{L}_{\text{signal}} \times \mathcal{L}_{\text{single-lepton}} \times \mathcal{L}_{\text{dilepton}} \} \times \mathcal{L}_{\text{nuisances}} \\
&= \prod_i \left\{ \prod_{K=H,V} \mathcal{P}(d_{K,i} | T_{K,i}(\vec{\theta})) \times \prod_{\ell=e,\mu} \mathcal{P}(d_{\ell\gamma,i} | T_{\ell\gamma,i}(\vec{\theta})) \times \prod_{\ell=e,\mu} \mathcal{P}(d_{\ell\ell\gamma,i} | T_{\ell\ell\gamma,i}(\vec{\theta})) \right\} \times \prod_j \mathcal{N}(\theta_j) \\
&= \prod_i \left\{ \prod_{K=H,V} \mathcal{P}\left(d_{K,i} \left| \left(1 + f_{W\gamma,i}^{Z\gamma}{}^{-1}(\vec{\theta})\right) C_K N_i^{Z\gamma} + h n_{K,i}^{\text{halo}}(\vec{\theta}) + C_K b_{K,i}(\vec{\theta}) \right.\right) \right. \\
&\quad \times \prod_{\ell=e,\mu} \mathcal{P}\left(d_{\ell\gamma,i} \left| \frac{N_i^{Z\gamma}}{R_{\ell\gamma,i}^{W\gamma}(\vec{\theta}) f_{W\gamma,i}^{Z\gamma}(\vec{\theta})} + b_{\ell\gamma,i}(\vec{\theta}) \right.\right) \\
&\quad \times \prod_{\ell=e,\mu} \mathcal{P}\left(d_{\ell\ell\gamma,i} \left| \frac{N_i^{Z\gamma}}{R_{\ell\ell\gamma,i}^{Z\gamma}(\vec{\theta})} + b_{\ell\ell\gamma,i}(\vec{\theta}) \right.\right) \left. \right\} \times \prod_j \mathcal{N}(\theta_j), \tag{1.4}
\end{aligned}$$

following the notation introduced in Section 1.2, and where $\mathcal{P}(n|\lambda)$ is the Poisson probability of n for mean λ , \mathcal{N} denotes the unit normal distribution, and $d_{X,i}$ is the observed number of events in bin i of region X . Systematic uncertainties are treated as nuisance parameters in the fit and are represented by $\vec{\theta}$. Each quantity Q_j with a nominal value \bar{Q}_j and a standard deviation of the systematic uncertainty σ_j appears in the likelihood function as $\bar{Q}_j \exp(\sigma_j \theta_j)$.

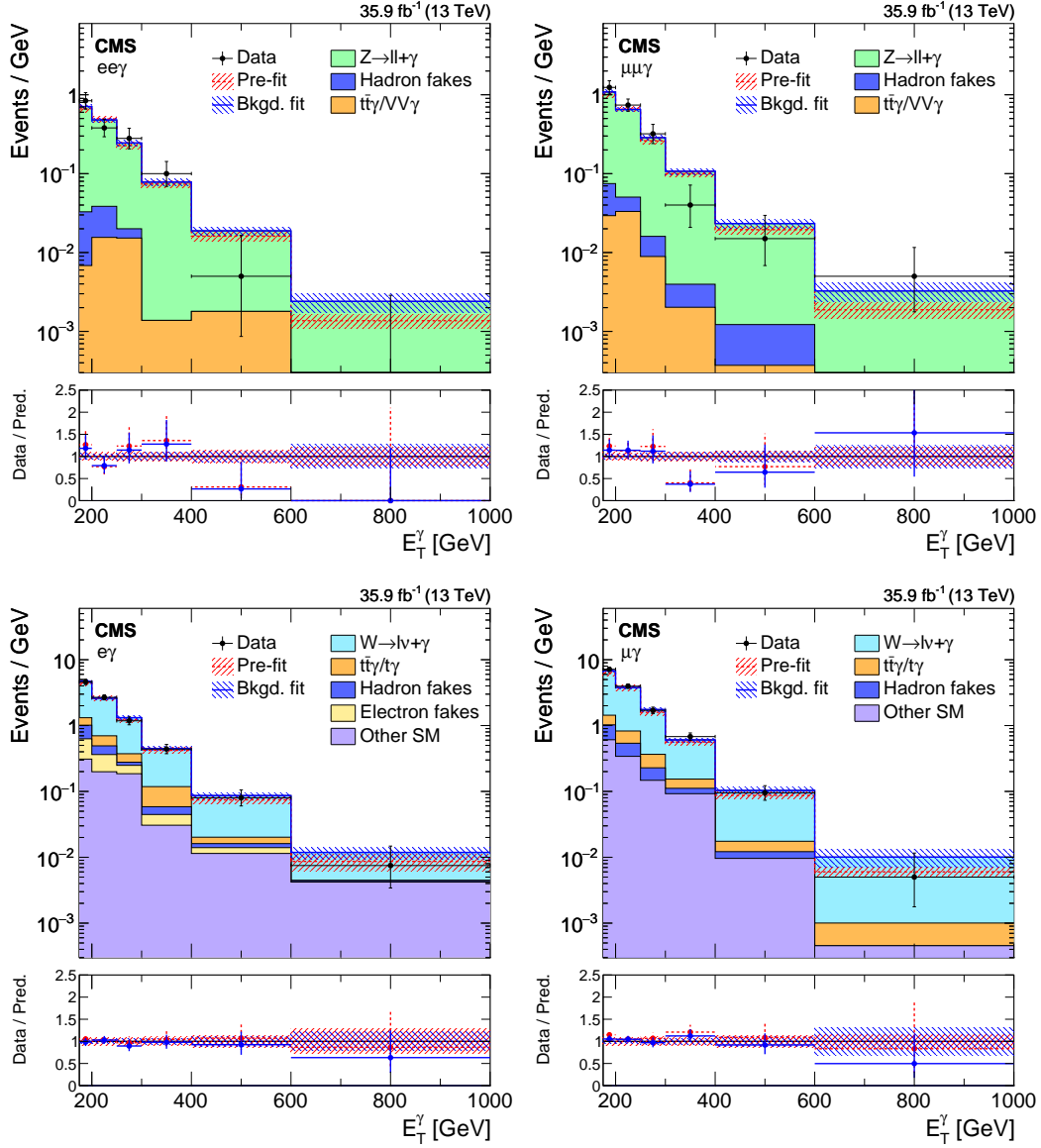


Figure 1-13: Comparison between data and MC simulation in the four control regions: $ee\gamma$ (upper left), $\mu\mu\gamma$ (upper right), $e\gamma$ (lower left), $\mu\gamma$ (lower right) before and after performing the simultaneous fit across all the control samples and signal region, and assuming absence of any signal. The last bin of the distribution includes all events with $E_T^\gamma > 1000$ GeV. The ratios of data with the pre-fit background prediction (red dashed) and post-fit background prediction (blue solid) are shown in the lower panels. The bands in the lower panels show the post-fit uncertainty after combining all the systematic uncertainties.

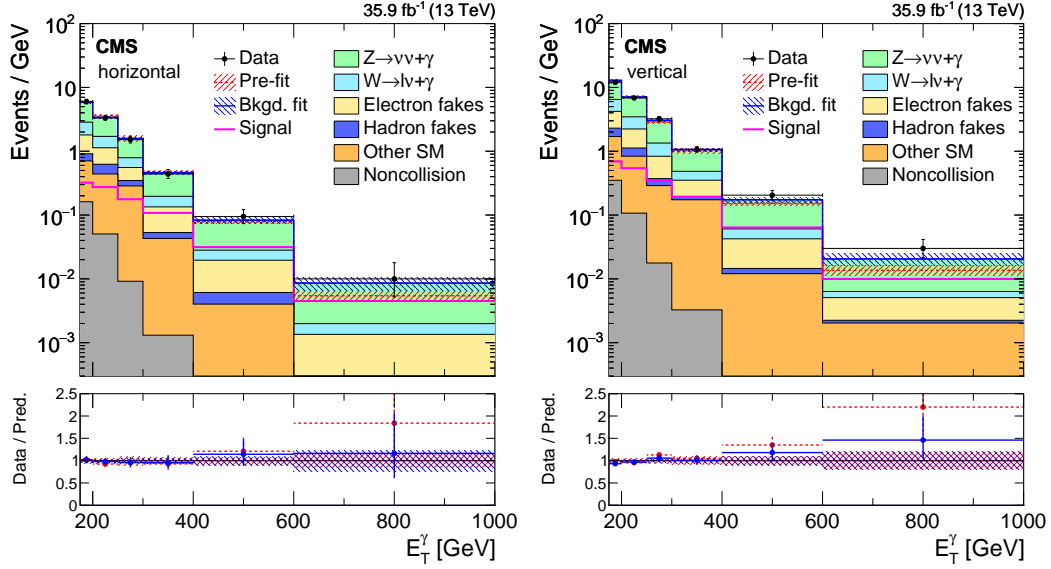


Figure 1-14: Observed E_T^γ distributions in the horizontal (left) and vertical (right) signal regions compared with the post-fit background expectations for various SM processes. The last bin of the distribution includes all events with $E_T^\gamma > 1000$ GeV. The expected background distributions are evaluated after performing a combined fit to the data in all the control samples and the signal region. The ratios of data with the pre-fit background prediction (red dashed) and post-fit background prediction (blue solid) are shown in the lower panels. The bands in the lower panels show the post-fit uncertainty after combining all the systematic uncertainties. The expected signal distribution from a 1 TeV vector mediator decaying to 1 GeV DM particles is overlaid.

1.9 Results

1.9.1 Pre-fit and post-fit distributions

Figure 1-13 shows the observed E_T^γ distributions in the four control regions compared with the results from simulations before and after performing the simultaneous fit across all the control samples and signal region, and assuming absence of any signal. Figure 1-14 shows the observed E_T^γ distributions in the horizontal and vertical signal regions compared with the results from simulations before and after performing a combined fit to the data in all the control samples and the signal region. The observed distributions are in agreement with the prediction from SM and noncollision backgrounds.

Table 1.2: Expected event yields in each E_T^γ bin for various background processes in the horizontal signal region. The background yields and the corresponding uncertainties are obtained after performing a combined fit to data in all the control samples, excluding data in the signal region. The observed event yields in the horizontal signal region are also reported.

E_T^γ [GeV]	[175, 200]	[200, 250]	[250, 300]	[300, 400]	[400, 600]	[600, 1000]
$Z\gamma$	81.2 ± 8.0	88.2 ± 8.4	38.8 ± 4.8	26.8 ± 3.7	8.8 ± 1.9	1.4 ± 0.7
$W\gamma$	27.9 ± 3.7	29.9 ± 3.9	11.4 ± 1.7	6.3 ± 1.2	1.4 ± 0.4	0.1 ± 0.1
Misid. electrons	22.5 ± 2.7	25.7 ± 2.7	10.5 ± 1.0	8.2 ± 0.7	2.7 ± 0.2	0.5 ± 0.0
Misid. hadrons	5.2 ± 2.2	9.3 ± 1.8	3.1 ± 0.7	1.0 ± 0.3	0.4 ± 0.1	0.0 ± 0.0
Other SM	13.6 ± 2.0	19.6 ± 1.3	13.9 ± 0.4	4.2 ± 0.2	0.8 ± 0.0	0.1 ± 0.0
ECAL spikes	4.3 ± 1.3	2.7 ± 0.8	0.5 ± 0.1	0.1 ± 0.0	0.0 ± 0.0	0.0 ± 0.0
Total prediction	154.6 ± 8.3	175.4 ± 8.8	78.2 ± 5.3	46.6 ± 4.0	14.1 ± 2.1	2.1 ± 0.8
Observed	150 ± 12	166 ± 13	76.0 ± 8.7	44.0 ± 6.6	19.0 ± 4.4	4.0 ± 2.0

The expected yields in each bin of E_T^γ for all backgrounds in the horizontal and vertical signal regions after performing a combined fit to data in all the control samples, excluding data in the signal regions, are given in Tables 1.2 and 1.3, respectively. The covariances between the predicted background yields across all the E_T^γ bins in the two signal regions are shown in Fig. 1-15. The expected yields together with the covariances can be used with the simplified likelihood approach detailed in Ref. [?] to reinterpret the results for models not studied in this thesis

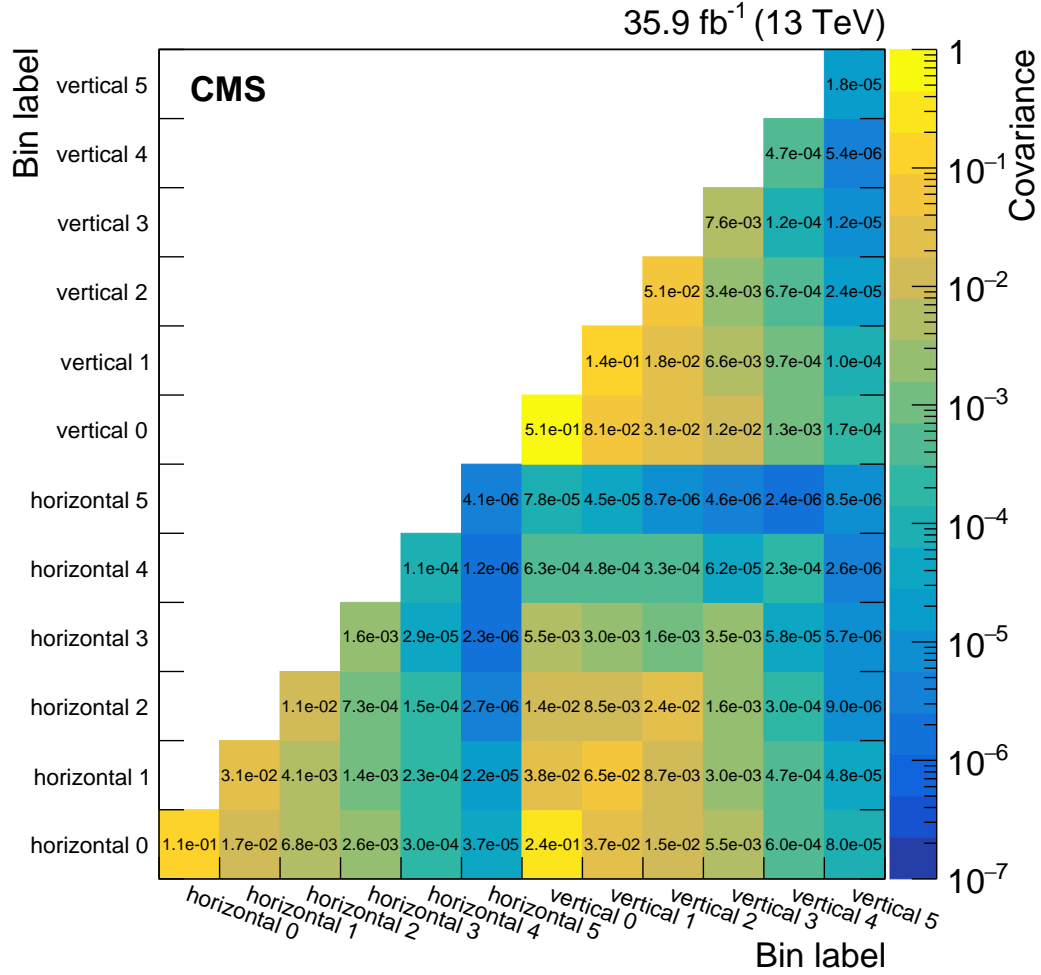


Figure 1-15: Covariances between the predicted background yields in all the E_T^γ bins of the horizontal and vertical signal regions. The bin labels specify which signal region the bin belongs to and what number bin it is for that region.

Table 1.3: Expected event yields in each E_T^γ bin for various background processes in the vertical signal region. The background yields and the corresponding uncertainties are obtained after performing a combined fit to data in all the control samples, excluding data in the signal regions. The observed event yields in the vertical signal region are also reported.

E_T^γ [GeV]	[175, 200]	[200, 250]	[250, 300]	[300, 400]	[400, 600]	[600, 1000]
$Z\gamma$	172 ± 17	190 ± 18	83 ± 10	58.6 ± 7.9	18.0 ± 3.9	3.1 ± 1.6
$W\gamma$	59.9 ± 7.8	63.6 ± 7.8	24.6 ± 3.5	13.4 ± 2.4	3.0 ± 0.8	0.3 ± 0.2
Misid. electrons	48.4 ± 5.6	56.2 ± 5.1	23.4 ± 1.8	15.7 ± 1.4	5.6 ± 0.4	1.2 ± 0.1
Misid. hadrons	15.1 ± 4.4	14.5 ± 3.1	4.2 ± 0.8	2.3 ± 0.8	0.5 ± 0.1	0.1 ± 0.1
Other SM	33.8 ± 4.1	36.6 ± 2.7	13.6 ± 0.5	17.1 ± 0.6	2.4 ± 0.1	0.8 ± 0.0
ECAL spikes	9.3 ± 2.8	5.7 ± 1.7	0.9 ± 0.3	0.3 ± 0.1	0.0 ± 0.0	0.0 ± 0.0
Total prediction	339 ± 18	366 ± 19	150 ± 11	107.5 ± 8.7	29.6 ± 4.3	5.4 ± 1.7
Observed	301 ± 17	342 ± 19	161 ± 13	107 ± 10	41.0 ± 6.4	12.0 ± 3.5

1.9.2 Limits

Figure 1-16 shows the 95% CL upper cross section limits with respect to the corresponding theoretical cross section ($\mu_{95} = \sigma_{95\%}/\sigma_{\text{theory}}$) for the vector and axial-vector mediator scenarios, in the $M_{\text{med}}-m_{\text{DM}}$ plane. The solid black (dashed red) curves are the observed (expected) contours of $\mu_{95} = 1$. The σ_{theory} hypothesis is excluded at 95% CL or above in the region with $\mu_{95} < 1$. The uncertainty in the expected upper limit includes the experimental uncertainties. For the simplified DM LO models considered, mediator masses up to 950 GeV are excluded for values of m_{DM} less than 1 GeV.

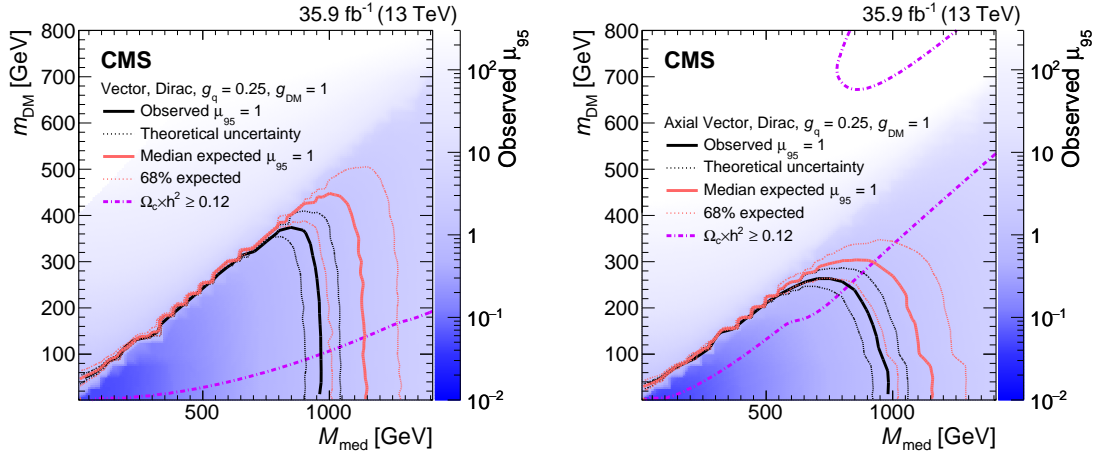


Figure 1-16: The ratio of 95% CL upper cross section limits to the theoretical cross section (μ_{95}), for DM simplified models with vector (left) and axial-vector (right) mediators, assuming $g_q = 0.25$ and $g_{\text{DM}} = 1$. Expected $\mu_{95} = 1$ contours are overlaid in red. The region under the observed contour is excluded. For DM simplified model parameters in the region below the lower violet dot-dash contour, and also above the corresponding upper contour in the right hand plot, cosmological DM abundance exceeds the density observed by the Planck satellite experiment.

Chapter 2

Comparison with Other Results

We're not doing this in a vacuum.

2.1 Monophoton

2.2 Monojet / Mono- Z

2.3 Direct Detection

We show the results in Fig. 2-1.

2.4 Indirect Detection

We show the results in Fig. 2-2.

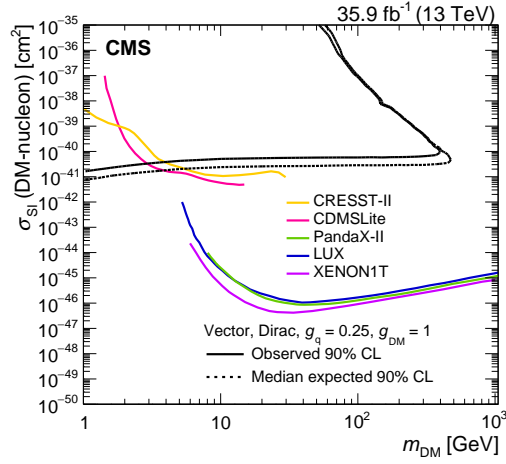


Figure 2-1: The 90% CL exclusion limits on the χ -nucleon spin-independent scattering cross sections involving the vector operator as a function of the m_{DM} . Simplified model DM parameters of $g_q = 0.25$ and $g_{\text{DM}} = 1$ are assumed. The region to the upper left of the contour is excluded. On the plots, the median expected 90% CL curve overlaps the observed 90% CL curve. Also shown are corresponding exclusion contours, where regions above the curves are excluded, from the recent results by the CDMSlite [?], LUX [?], PandaX-II [?], XENON1T [?], and CRESST-II [?].

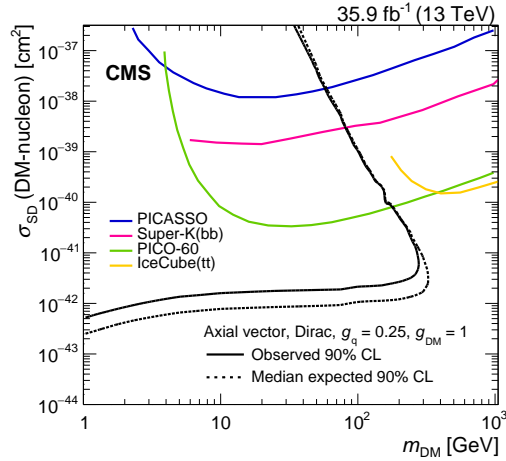


Figure 2-2: The 90% CL exclusion limits on the χ -nucleon spin-dependent scattering cross sections involving the axial-vector operator as a function of the m_{DM} . Simplified model DM parameters of $g_q = 0.25$ and $g_{\text{DM}} = 1$ are assumed. The region to the upper left of the contour is excluded. On the plots, the median expected 90% CL curve overlaps the observed 90% CL curve. Also shown are corresponding exclusion contours, where regions above the curves are excluded, from the recent results by the PICO-60 [?], IceCube [?], PICASSO [?] and Super-Kamiokande [?] Collaborations.